Generalized superlattice K·p theory and intersubband optical transitions

M. E. Flatté,* P. M. Young, L.-H. Peng, and H. Ehrenreich†
Division of Applied Sciences, Harvard University, Cambridge, Massachusetts 02138
(Received 28 July 1995)

The eight-band superlattice crystal $\mathbf{K}\cdot\mathbf{p}$ formalism is extended to include the higher-lying antibonding p states perturbatively. The initial 14×14 Hamiltonian matrix is block diagonalized (or folded down) so that corrections due to these states appear in the modified 8×8 matrix. Their principal effect is to introduce a finite heavy-hole mass. The use of the eight-band formalism for band-structure and interband optical calculations is validated because other corrections are very small. The approximate wave functions associated with the original 14×14 Hamiltonian are used to calculate intersubband optical matrix elements. These include new terms, present in crystals lacking inversion symmetry, which increase the magnitude of conduction intersubband absorption by about three orders of magnitude for in-plane polarized (TE) photons, while leaving absorption due to growth-axis polarized (TM) photons relatively unaffected. The TE absorption in narrow GaAs/Al_xGa_{1-x}As quantum wells (QW's) is shown to be observable. However, use of the f-sum rule and the cyclotron-resonance-determined conduction-band effective-mass anisotropy indicate an upper limit of about 20% relative to TM absorption. Comparison with the measured TM absolute absorption coefficient for a system used for quantum-well infrared photoconductors (QWIP's) yields excellent agreement. The conductivity sum rule involving these intersubband transitions is used to confirm the observed broadening associated with very small QW width fluctuations for this system.

I. INTRODUCTION

Superlattice crystal $\mathbf{K}\cdot\mathbf{p}$ theory,[1–3] which is a reformulation of superlattice (SL) $\mathbf{k}\cdot\mathbf{p}$ theory,[4] has been used to explain the optoelectronic properties of a variety of III-V (Refs. 5 and 6) and II-VI (Refs. 7 and 8) compounds and superlattices with a view toward exploring the materials physics underpinning IR detectors, lasers and, more generally, the detailed optical properties of semiconductor heterostructures including excitons.[5,8,9] This theory is posited on the fact that ideal superlattices are perfectly periodic, albeit highly anisotropic solids so that the wave vector $\mathbf{K}$ pertains to the SL rather than the bulk constituents. The consequence that Bloch's theorem applies can therefore be used to reformulate the SL $\mathbf{k}\cdot\mathbf{p}$ theory as originally proposed by Bastard[4] in a simpler and more elegant form.

This paper extends the theory from the original 8 bands to a 14-band model which specifically includes the antibonding conduction p (or $\bar{p}$) states in addition to the lowest two s conduction and the six uppermost p valence bands. The effects of the $\bar{p}$ states are principally to produce curvature in the heavy-hole (HH) bands and to modify the momentum matrix elements coupling the various bands. This modification results from the 14-component wave functions that replace the earlier 8-component wave functions. The effects are substantial for conduction intersubband transitions, but leave interband (valence to conduction) transitions largely unaffected.

The 14×14 Hamiltonian matrix is block diagonalized (folded down) into 8×8 $p\bar{s}$ and 6×6 $\bar{p}$ matrices and used perturbatively to show that the matrix elements coupling the $p\bar{s}$ states through the $\bar{p}$ states have a small effect on the energy eigenvalues computed for the 8×8 case if the input parameters are determined semiempirically as in previous work. Folding down to an 8×8, followed by exact diagonalization, appears to be unique to this work. The folding-down procedure has been used by others[10] for bulk semiconductors to reduce the 14×14 Hamiltonian to a perturbative 2×2 Hamiltonian, primarily to evaluate magnetic-field effects, especially the fine structure of cyclotron resonance.

Our earlier calculations assumed the *bulk* constituents of the SL to have band gaps E_g and conduction and heavy-hole masses m_C and m_{HH}, respectively, which are known experimentally. The band offsets and strain effects of the resulting SL were also treated semiempirically. The calculated interband optical absorption including exciton effects was seen to be in excellent agreement with experiment with respect to both structure and magnitude if the line broadening is assumed to result from a $\pm$ single-layer fluctuation in the interface.[6] (For the II-VI systems it was also necessary to assume a modest 2–3 % alloy composition fluctuation to obtain quantitative agreement.[8]) Nonparabolic band effects are included since the original or folded-down 8×8 matrix is fully diagonalized without further approximations. The folding-down procedure therefore justifies the 8×8 matrix used in previous calculations.[1–3,5–9]

In addition to the theoretical developments just described (Sec. II and the Appendixes contain specific details), this paper explores optical intersubband transitions from the lowest conduction subband $C1$ to higher ones Cn $(n=2-5)$ (Sec. IV). These transitions are basic to the operation of quantum-well infrared photodetectors (QWIP's) used as IR detectors,[11,12] and a proposal for a charge-activated optical modulation device (CALM) made some years ago.[13] Moreover, as emphasized in this group's first paper[1] concerning the SL f-sum rule, the existence of a strong $C1\rightarrow C2$ transition for the transverse magnetic mode (TM; light polarized along the SL growth axis) compared to a transverse electric mode (TE; light polarized in the SL plane perpendicular to the growth axis) which is 10^4-10^5 times smaller, is quanti-

tatively responsible for the crystal SL effective-mass anisotropy observed in cyclotron resonance experiments.[14]

This question is revisited here in connection with recent claims[15,16] that the TE and TM optical absorption have comparable magnitudes. If correct, this claim would allow QWIP's to be used in the normal-incidence configuration without the use of diffraction gratings, which does not appear to be the case. Furthermore, the effective-mass anisotropies would be substantially eliminated.

The TE transition is allowed for $\mathbf{K}=\mathbf{0}$ in the presence of spin-orbit interactions and is greatly enhanced when the bulk SL constituents lack inversion symmetry. Peng and Fonstad[17] utilized this latter ingredient, which had been previously neglected, to argue that the observed large TE absorption is associated with a momentum matrix element P_1, to be defined in Sec. II, which is present in zinc blende but not in diamond structures, and leads to nonlinear optical absorption in lowest order. Peng and Fondstad's additional claim that the matrix element Q vanished in diamond symmetry is incorrect, as pointed out most recently in Ref. 18. Nevertheless, their argument that the reduction in symmetry from diamond to zinc blende greatly enhances TE absorption can be tested. This reduction, and the resulting momentum matrix element P_1, which appears explicitly in the 14-band model, indeed increases the TE absorption in GaAs- and $In_xGa_{1-x}As$-based QW's by 2–3 orders of magnitude. Despite this enhancement, the TE absorption remains 5–10 times smaller than that associated with the TM mode. As pointed out in Sec. IV B, however, the TE mode should be experimentally observable in narrow ($\sim$40 Å) GaAs quantum wells (QW's). In these wells the TE absorption is about 20% of that due to TM. We present arguments based on f and conductivity sum rules that indicate that the 20% figure is likely to be an upper limit for QW's in which $C1$ is a localized state and Cn $(n\geqslant 2)$ lie in the continuum.

This paper presents absorption results for the $C1\rightarrow\Sigma_n Cn$ $(2\leqslant n\leqslant 5)$ transitions in a $GaAs/Al_xGa_{1-x}As$ quantum well relevant to the QWIP case, and shows that the results agree quantitatively with the experiments of the Levine group.[11] The excited states $(n\geqslant 2)$ all lie energetically near or in the continuum. The momentum matrix elements are shown to be larger than for transitions involving localized final states. This is the case for the $C1\rightarrow C2$ transition relevant to CALM,[13] where $C2$ lies in the well. This system is reexamined here for two GaAs QW's having different widths to confirm that the large and extremely sharp optical absorption is associated with the density of states enhancement resulting from optimal nesting of the $C1$ and $C2$ bands.

The 14×14 results for the three $GaAs/Al_xGa_{1-x}As$ systems for light polarized in the TM mode are in better agreement with experiment than those of the 8×8 results because of the aforementioned changes in momentum matrix elements. Furthermore, as expected, the 8×8 TE absorption is 3–4 orders smaller than the TM absorption because the effects associated with P_1 are neglected.

II. DERIVATION OF THE EFFECTIVE EIGHT-BAND BULK HAMILTONIAN

The Hamiltonian appropriate for the bulk constituents of superlattices and quantum wells treated here is

$$H(\mathbf{r})=\frac{\mathbf{p}^2}{2m}+V(\mathbf{r})+\frac{\hbar}{4m^2c^2}[\sigma\times\nabla V(\mathbf{r})]\cdot\mathbf{p}, \qquad (2.1)$$

where m is the free-electron mass, c is the velocity of light, $\mathbf{p}$ is the electron momentum, and $V(\mathbf{r})$ is the crystal potential. This group's previous work calculating optical properties of superlattice relied on a semiempirical parametrization of the bulk constituents within a modified Kane or eight-band model, consisting of six valence (bonding) p states and two conduction (antibonding) s states $(\bar{s})$.[2] This paper will generalize the eight-band model by considering the influence of the most important previously neglected six antibonding p states $(\bar{p})$ by folding them down into the eight-band basis set using standard procedures.[19] The corrections are generally small, and the earlier model that has been used extensively with considerable success is therefore valid. In order to calculate momentum matrix elements it will be necessary to unfold the approximated 8-component wave function to reconstruct the approximate 14-component wave function. The strategy is delineated in Fig. 1, and will be summarized after the procedure has been described in full.

These 14 bands are shown schematically in Fig. 2. The parameters defining a bulk system in $\mathbf{k}\cdot\mathbf{p}$ perturbation theory are also indicated: E_c is the energy separation between the $\bar{s}$ and $\bar{p}$ states; E_g is the fundamental gap (between $\bar{s}$ and p); Δ and Δ_c, respectively, are the spin-orbit splitting between the p and $\bar{p}$ states. The energy zero is taken as the maximum of the highest valence band (HH). Three momentum matrix elements

$$\begin{aligned} P_0&=-i\sqrt{2/3}\langle S|p_z|Z^v\rangle,\\ P_1&=-i\sqrt{2/3}\langle S|p_z|Z^c\rangle, \qquad (2.2)\\ Q&=-i\sqrt{2/3}\langle X^v|p_y|Z^c\rangle=i\sqrt{2/3}\langle X^c|p_y|Z^v\rangle \end{aligned}$$

couple the states away from the zone center in the $\mathbf{k}\cdot\mathbf{p}$ formalism. All three are real. In a solid having inversion symmetry $P_1=0$. The presence of a nonzero P_1 is associated with the zinc-blende symmetry in the present case.[20]

The folding-down procedure to be used here is valid if the six $\bar{p}$ states to be folded into the eight $p\bar{s}$ states do not energetically coincide with the latter. Although the procedure is exact in the present case for sufficiently small k, second-order expressions will be sufficient to incorporate the effect of the $\bar{p}$ states on the eight-band basis.

The 14-band Hamiltonian has the following schematic form:

$$H=\begin{bmatrix} H_{p\bar{s}} & H_{p\bar{s}\text{-}\bar{p}} \\ (8\times 8) & (8\times 6) \\ H^{\dagger}_{p\bar{s}\text{-}\bar{p}} & H_{\bar{p}} \\ (6\times 8) & (6\times 6) \end{bmatrix}, \qquad (2.3)$$

where p and $\bar{s},\bar{p}$ denote bonding and antibonding states, respectively. The full constituent matrices and the 14 basis functions are given in Appendix A. As indicated in Eqs. (A1) and (A2), the diagonal elements of $H_{p\bar{s}}$ consist of the zone-center energies of the eight $\bar{s}$ and $\bar{p}$ states. The eight off-diagonal elements connect the $\bar{s}$ and p states. $H_{p\bar{s}\text{-}\bar{p}}$ consists entirely of $\mathbf{k}\cdot\mathbf{p}$ matrix elements connecting the $p\bar{s}$ states and

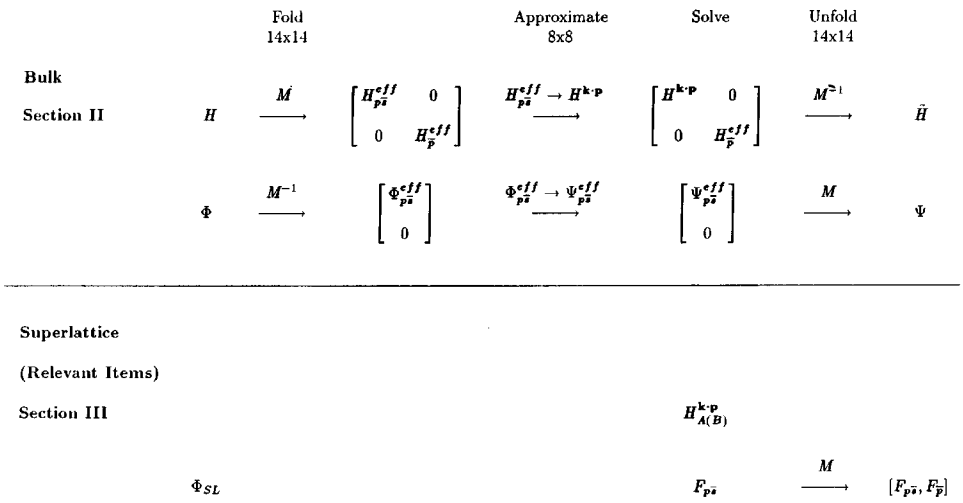

FIG. 1. Schematic of the folding-down and approximation procedures for calculating eigenstates. A 14-band bulk Hamiltonian H [Eq. (A1)] is folded down into an 8-band $H^{\rm eff}_{p\bar{s}}$ [Eq. (A6)]. Eigenstates Φ of H correspond to eight-component eigenstates $\Phi^{\rm eff}_{p\bar{s}}$ of $H^{\rm eff}_{p\bar{s}}$ [Eqs. (2.8) and (2.9)]. Approximations are necessary to arrive at the 8-band $H^{\mathbf{k}\cdot\mathbf{p}}$[Eq. (2.13)], with associated approximate eigenfunctions $\Psi^{\rm eff}_{p\bar{s}}$. In order to calculate momentum matrix elements, $\Psi^{\rm eff}_{p\bar{s}}$ must be unfolded to yield Ψ [via Eqs. (2.8) and (2.9)]. For the superlattice the $\mathbf{F}_{p\bar{s}}$ are the envelope functions for the 8-band superlattice Hamiltonian $H^{\mathbf{k}\cdot\mathbf{p}}_{A(B)}$ [Eq. (3.15)] which corresponds to the bulk $H^{\mathbf{k}\cdot\mathbf{p}}$. The 14 components of $\mathbf{F}$ [Eqs. (3.11)–(3.13)] are necessary to calculate momentum-matrix elements.

the $\bar{p}$ states, and is therefore proportional to $\mathbf{k}$. In particular, $H_{p\bar{s}\text{-}\bar{p}}$ depends on P_1, which couples $\bar{s}$ and $\bar{p}$ states as allowed in crystals lacking inversion symmetry, and also Q. $H_{\bar{p}}$ is a diagonal matrix whose elements are the zone-center energies of the $\bar{p}$ states.

To implement the folding-down or block diagonalization procedure,[21] we consider the Schrödinger equation in the form $(H-E)\Phi=0$. Inserting a matrix

$$M=\begin{pmatrix} I & -(H_{p\bar{s}}-E)^{-1}H_{p\bar{s}\text{-}\bar{p}} \\ -(H_{\bar{p}}-E)^{-1}H^{\dagger}_{p\bar{s}\text{-}\bar{p}} & I \end{pmatrix} \tag{2.4}$$

and its inverse yields $(H-E)MM^{-1}\Phi=0$, or, explicitly,

$$\begin{pmatrix} H^{\rm eff}_{p\bar{s}}-E & 0 \\ 0 & H^{\rm eff}_{\bar{p}}-E \end{pmatrix}\Phi^{\rm eff}=0, \tag{2.5}$$

where

$$\Phi^{\rm eff}=M^{-1}\Phi \tag{2.6}$$

and

$$\begin{aligned} H^{\rm eff}_{p\bar{s}}-E &= H_{p\bar{s}}-E-H_{p\bar{s}\text{-}\bar{p}}(H_{\bar{p}}-E)^{-1}H^{\dagger}_{p\bar{s}\text{-}\bar{p}} \\ &= H_{p\bar{s}}-E+\delta H_{p\bar{s}}. \end{aligned} \tag{2.7}$$

The structure of Eq. (2.5) implies that the 14-component $\Phi^{\rm eff}$ is composed of an 8-component $\Phi^{\rm eff}_{p\bar{s}}$ and a 6-component $\Phi^{\rm eff}_{\bar{p}}$. Specifically,

$$\Phi_{p\bar{s}}=\Phi^{\rm eff}_{p\bar{s}} \tag{2.8}$$

and

$$\Phi_{\bar{p}}=-(H_{\bar{p}}-E)^{-1}H^{\dagger}_{p\bar{s}\text{-}\bar{p}}\Phi_{p\bar{s}}. \tag{2.9}$$

Solutions of interest to Eq. (2.5) have $\Phi^{\rm eff}_{\bar{p}}=0$.

The detailed form of $\delta H_{p\bar{s}}$ is given in Appendix A in Eqs. (A1) and (A6). $\delta H_{p\bar{s}}$ depends on $H_{p\bar{s}\text{-}\bar{p}}$ and hence explicitly on k^2 [cf. Eq. (A4)]. E, however, also depends on k. Note that the rows and columns of the matrix appearing in Eq. (A6) are labeled sequentially by the states C (conduction), LH (light hole), HH (heavy hole), and SO (split-off band). The folding-down procedure has been followed without approximation to this point.

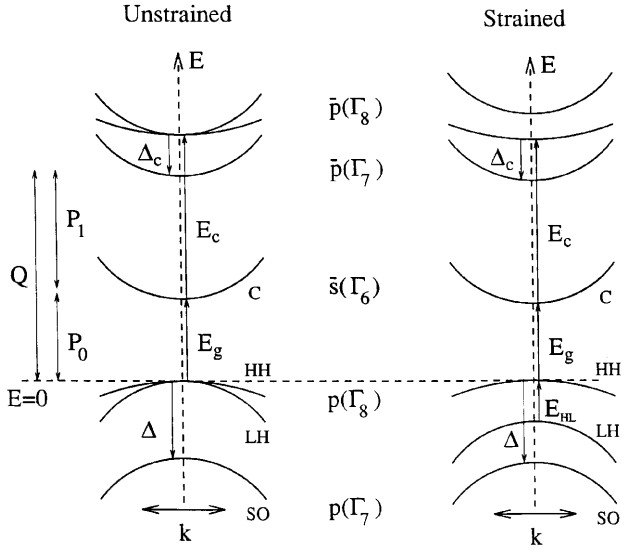

FIG. 2. The 14 bulk bands considered: 6 p states, 2 $\bar{s}$ states, and 6 $\bar{p}$ states ($\bar{s}$ indicates antibonding s states). Four energies define the unstrained zone-center bands: E_g, the $\bar{s}-p$ energy difference; E_c, the $\bar{s}-\bar{p}$ energy difference; and the spin-orbit splittings Δ and Δ_c among the p and $\bar{p}$ states, respectively. The strained structure on the right has altered values of these four energies, as well as two additional splittings: $E_{\rm HL}$, between the heavy and light p states, and a splitting not labeled between the heavy and light $\bar{p}$ states.

We now consider expressions for $\delta H_{p\bar{s}}$ in second-order perturbation theory, which will be seen to suffice for the present purposes. This approximation consists of replacing E by the zone-center energy of the relevant band, and is valid when the $\bar{p}$ states are energetically well separated from the $p\bar{s}$ states. The resulting changes in the band structure are primarily proportional to k^2. Additional terms are seen to appear, coupling the heavy-hole and conduction bands and the light-hole and split-off bands. These terms are small. The magnitude of the heavy-hole–conduction coupling is given by the (3,1) matrix element of Eq. (A6), with E replaced by 0 (the location of the valence-band maximum):

$$\frac{\hbar^2k^2}{\sqrt{2}m}\frac{P_1Q}{m}\left[\frac{1}{(E_c+E_g-\Delta_c)}-\frac{1}{(E_c+E_g)}\right]. \tag{2.10}$$

Its magnitude for $k=0.1$ Å^{-1}, typical for electrons in a bulk room-temperature semiconductor, or the Brillouin-zone extent of a 30-Å superlattice, is approximately 2 meV for GaAs. Similarly, the light-hole–split-off coupling [element (2,4) with E replaced by 0] is

$$\frac{\hbar^2k^2}{\sqrt{2}m}\frac{Q^2}{m[(E_c+E_g)]}. \tag{2.11}$$

Its value for $k=0.1$ Å^{-1} is approximately 50 meV. These couplings are quite small, particularly for the heavy-hole–conduction case. The energy shifts resulting from these couplings have magnitudes of 10^{-3} and 5 meV, respectively, at $k=0.1$ Å^{-1}, and depend to lowest order on k^4.

Previous work neglected the $\bar{p}$ bands except for an empirical coupling term providing a finite effective mass to the HH band, which corresponds to the (3,3) element of Eq. (A6) for $E=0$:

$$\frac{m}{m_{\rm HH}}=1-\frac{Q^2(3E_c+3E_g-\Delta_c)}{m(E_c+E_g)(E_c+E_g-\Delta_c)}. \tag{2.12}$$

If the term involving the free-electron mass and coupling terms (2.10) and (2.11) of $h_{p\bar{s}}^{\rm eff}$ are neglected, but the (3,3) matrix element giving rise to the heavy-hole mass term is retained, $h_{p\bar{s}}^{\rm eff}$ reduces to the 8×8 $\mathbf{k}\cdot\mathbf{p}$ Hamiltonian

$$h^{\mathbf{k}\cdot\mathbf{p}}=\begin{pmatrix} E_g & \frac{iP_0\hbar k}{m} & 0 & \frac{iP_0\hbar k}{\sqrt{2}m} \\ -\frac{iP_0\hbar k}{m} & 0 & 0 & 0 \\ 0 & 0 & -\frac{\hbar^2k^2}{2m_{\rm HH}} & 0 \\ -\frac{iP_0\hbar k}{\sqrt{2}m} & 0 & 0 & -\Delta \end{pmatrix} \tag{2.13}$$

used in previous work. $H_{p\bar{s}}$ is defined in terms of $h_{p\bar{s}}$ by Eq. (A1). The first eight bulk $\mathbf{k}=\mathbf{0}$ $p\bar{s}$ basis states $|n,0\rangle$ are defined in Table I in terms of the states $|S\rangle$, $|X\rangle$, $|Y\rangle$, and $|Z\rangle$ in the notation of Ref. 2. (Note that Table I also includes the $\bar{p}$ states expressed in terms of the states $|X^C\rangle$, $|Y^C\rangle$, and $|Z^C\rangle$ in the notation in Ref. 22.)

TABLE I. Bulk modified Kane model $\mathbf{k}=\mathbf{0}$ states $|n,0\rangle$ for the Γ_6 bulk band edge and the bonding and antibonding Γ_7 and Γ_8 bulk band edges. The notation of Refs. 2 and 22 is used. The ordering of these states ensures that the matrices discussed in the Appendices are block diagonal.

	$n:\lvert n,0\rangle$
Γ_6	$1:\lvert S_\uparrow\rangle$
Γ_8	$2:\lvert\sqrt{2/3}\rvert Z_\uparrow\rangle-\sqrt{1/6}\rvert X_\downarrow+iY_\downarrow\rangle$
	$3:\sqrt{1/2}\rvert X_\downarrow-iY_\downarrow\rangle$
Γ_7	$4:\sqrt{1/3}\rvert Z_\uparrow\rangle+\sqrt{1/3}\rvert X_\downarrow+iY_\downarrow\rangle$
Γ_6	$5:\lvert S_\downarrow\rangle$
Γ_8	$6:\sqrt{2/3}\rvert Z_\downarrow\rangle+\sqrt{1/6}\rvert X_\uparrow-iY_\uparrow\rangle$
	$7:\sqrt{1/2}\rvert X_\uparrow+iY_\uparrow\rangle$
Γ_7	$8:\sqrt{1/3}\rvert Z_\downarrow\rangle-\sqrt{1/3}\rvert X_\uparrow-iY_\uparrow\rangle$
Γ_8	$9:\sqrt{2/3}\rvert Z_\uparrow^c\rangle-\sqrt{1/6}\rvert X_\downarrow^c+iY_\downarrow^c\rangle$
	$10:\sqrt{1/2}\rvert X_\downarrow^c-iY_\downarrow^c\rangle$
Γ_7	$11:\sqrt{1/3}\rvert Z_\uparrow^c\rangle+\sqrt{1/3}\rvert X_\downarrow^c+iY_\downarrow^c\rangle$
Γ_8	$12:\sqrt{2/3}\rvert Z_\downarrow^c\rangle+\sqrt{1/6}\rvert X_\uparrow^c-iY_\uparrow^c\rangle$
	$13:\sqrt{1/2}\rvert X_\uparrow^c+iY_\uparrow^c\rangle$
Γ_7	$14:\sqrt{1/3}\rvert Z_\downarrow^c\rangle-\sqrt{1/3}\rvert X_\uparrow^c-iY_\uparrow^c\rangle$

The preceding arguments lead to the important result that the non-folded-down (8×8) matrix involving $h^{\mathbf{k}\cdot\mathbf{p}}$ used in previous calculations[1–3,5–9] provides a quite accurate description of the band structure and thus justifies its semiempirical use. The semiempirical procedure used earlier was the following: the bulk systems for an eight-band model were parameterized by taking the values for E_g, Δ, m_C, and $m_{\rm HH}$ from experiment.[2] P_0 is determined from the zone-center conduction-band mass using

$$\frac{m}{m_C}=\frac{P_0^2(3E_g+2\Delta)}{mE_g(E_g+\Delta)}. \tag{2.14}$$

The free-electron mass term is neglected.

A similar method parametrizing the 14-band bulk system requires in addition the experimental values of E_c and Δ_c. Expressions for the masses of the four types of $p\bar{s}$ bands, conduction (C), heavy-hole (HH), light-hole (LH), and split off (SO), are found by replacing E in $\delta H_{p\bar{s}}$ with the zone-center energy of the relevant band:

$$\frac{m}{m_C}=1+\frac{P_0^2(3E_g+2\Delta)}{mE_g(E_g+\Delta)}-\frac{P_1^2(3E_c-2\Delta_c)}{mE_c(E_c-\Delta_c)}, \tag{2.15}$$

$$\frac{m}{m_{\rm HH}}=1-\frac{Q^2(3E_c+3E_g-\Delta_c)}{m(E_c+E_g)(E_c+E_g-\Delta_c)}, \tag{2.16}$$

$$\frac{m}{m_{\rm LH}}=1-\frac{2P_0^2}{mE_g}-\frac{Q^2}{m(E_c+E_g)}, \tag{2.17}$$

$$\frac{m}{m_{\rm SO}}=1-\frac{P_0^2}{m(E_g+\Delta)}-\frac{Q^2}{m(E_c+E_g+\Delta)}. \tag{2.18}$$

The masses in Eqs. (2.15)–(2.17) could be used to find the three momentum matrix elements from three experimental effective masses. This could lead to substantial error, however, since only m_C is experimentally well known, and fur-

TABLE II. Parameters for bulk 8-band and 14-band **k·p** band structures for GaAs. Our empirical parameters (Ref. 23) for 8-band and 14-band models, obtained as described in Sec. III, are compared with parameters from Ref. 22. E_g is the fundamental gap, E_c is the zone-center gap between $\bar{s}$ and $\bar{p}$ states, and Δ and Δ_c are the spin-orbit splitting for p and $\bar{p}$ states, respectively. m_{HH} is in units of the free-electron mass.

	8 bands	14 bands	Ref. 22
E_g (eV)	1.519	1.519	1.519
Δ (eV)	0.341	0.341	0.340
E_c (eV)	N/A	3.140	3.140
Δ_c (eV)	N/A	0.171	0.171
$E_{P_0}=2\lvert\langle S\rvert p_z\rvert Z^v\rangle\rvert^2/m$ (eV)	24.2	25.7	26.0
$E_{P_1}=2\lvert\langle S\rvert p_z\rvert Z^c\rangle\rvert^2/m$ (eV)	N/A	5.9	6.0
$E_Q=2\lvert\langle X^v\rvert p_y\rvert Z^c\rangle\rvert^2/m$ (eV)	N/A	13.5	12.0
m_{HH}	0.51	N/A	N/A

thermore depends only weakly on P_1 in Eq. (2.15). Therefore we will determine P_1 from a pseudopotential calculation by Cardona, Christensen, and Fasol[22] which yields $P_1=0.48P_0$ for GaAs. The experimental values of m_C and m_{HH} (Ref. 23) will then be used to determine P_0 and Q from Eqs. (2.15) and (2.16). The parameters for GaAs obtained from the two procedures are compared in Table II to the parameters used in Ref. 22. The Q's differ by 11%. The present 14-band model differs from experimental values for GaAs by 8% for m_{LH} and by 45% for m_{SO}.

Figure 3 shows the band structure for GaAs calculated with the previously used 8-band semiempirical parametrization as compared to the 14-band semiempirical parametrization presented here. As required by the parametrization methods, m_C and m_{HH} are the same for both. The percent difference in m_{LH} is 5% and in m_{SO} is 3%. The masses are more similar than might be expected because of counteracting effects of the terms in Eqs. (2.15)–(2.18) involving P_1 and Q. The most prominent difference in the band structures is that the approximation causes the heavy-hole band to cross the light-hole band in the 8-band model. This unphysical result shown in the vertically enlarged inset occurs at large

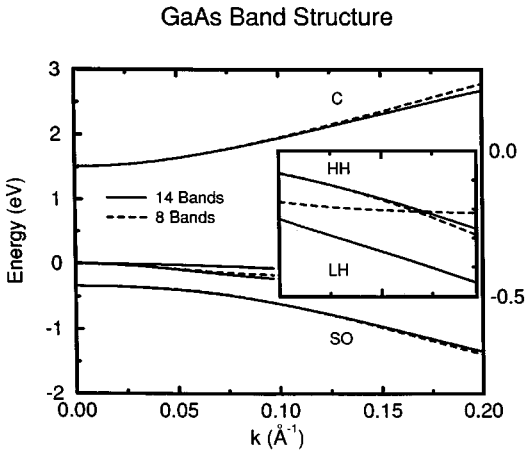

FIG. 3. Comparison of the bulk 14- and 8-band **k·p** models for GaAs. The inset shows a vertical blow-up of the region with the most significant differences ($k>0.1$ Å^{-1}).

$k=0.167$ Å^{-1}. We conclude that the bulk band structure resulting from the 8-band $H^{\mathbf{k}\cdot\mathbf{p}}$ is satisfactory for calculating superlattice band structures.

Figure 1 summarizes the strategy adopted in this calculation. The 14-band Hamiltonian H is block diagonalized (or folded down) into a Hamiltonian containing the 8-band matrix $H_{p\bar{s}}^{\mathrm{eff}}$ in a procedure defined by Eqs. (2.3)–(2.9), which is exact in principle. The 14-component eigenstates Φ of H correspond to 8-component eigenstates $\Phi_{p\bar{s}}^{\mathrm{eff}}$. The approximations to $H_{p\bar{s}}^{\mathrm{eff}}$ described above yield $H^{\mathbf{k}\cdot\mathbf{p}}$, and approximate eigenstates $\Psi_{p\bar{s}}^{\mathrm{eff}}$. The Schrödinger equation is solved at this point, yielding $\Psi_{p\bar{s}}^{\mathrm{eff}}$. Since the energies given by this procedure are extremely close to those of the 14-band model (see Fig. 3), the effects of the $\bar{p}$ states on intersubband absorption, the optical property of interest in this paper, will be dominated by their influence on the wave functions $\Psi_{p\bar{s}}^{\mathrm{eff}}$. In order to calculate momentum matrix elements for intersubband absorption, the 8-component $\Psi_{p\bar{s}}^{\mathrm{eff}}$ is unfolded to yield an approximate 14-component eigenstate Ψ. Ψ is related to $\Psi_{p\bar{s}}^{\mathrm{eff}}$ in the same way as Φ is related to $\Phi_{p\bar{s}}^{\mathrm{eff}}$ [i.e., via Eqs. (2.6), (2.8), and (2.9)]. The explicit form of the corresponding Hamiltonian H will not be needed. The superlattice part of Fig. 1 will be discussed in Sec. III.

In a non-lattice-matched superlattice the bulk constituents are strained. Strain affects the energy gap and splits the degeneracy of the light and heavy holes of a bulk material, as shown schematically in Fig. 2. The effect of strain is obtained from empirical lattice constants, elastic constants, and deformation potentials for bulk material, as well as the in-plane lattice constant $a_\parallel$ of the superlattice.[8] Effects on the momentum matrix elements P_0, P_1, or Q are neglected in the present treatment.

The hydrostatic strain e_H and biaxial strain e_B on a bulk material forced to conform to the in-plane lattice constant $a_\parallel$ are

$$e_H=2\left(1-\frac{c_{12}}{c_{11}}\right)e_\parallel, \quad e_B=\left(1+2\frac{c_{12}}{c_{11}}\right)e_\parallel, \tag{2.19}$$

where $e_\parallel=(a_\parallel-a)/a_\parallel$ is the in-plane strain, c_{11} and c_{12} are the elastic constants of the bulk material, and a is the lattice constant.

These strains influence the various gaps shown schematically in Fig. 2, particularly E_g and the heavy-hole–light-hole gap E_{HL}:

$$E_{g,\mathrm{strained}}=E_{g,\mathrm{unstrained}}+e_Hc-|e_Bb|, \tag{2.20}$$

$$E_{\mathrm{HL}}=2e_Bb-\frac{2(e_Bb)^2}{\Delta}.$$

Here c and b are deformation potentials.

III. SUPERLATTICE ELECTRONIC STRUCTURE

Since the bulk 8-band effective Hamiltonian adequately reproduces the 14-band electronic structure, the 8-band Hamiltonian will be used to obtain the superlattice (SL) electronic energy levels (but not the eigenstates). The effects of folding down the 14-band basis set, and the effects of strain,

are included in the bulk $\mathbf{k}\cdot\mathbf{p}$ formalism on which the SL treatment is based.

The superlattices considered are composed of alternating layers of two bulk semiconductors, designated A and B. The formalism yielding the superlattice band structure regards the SL as a perfectly periodic, highly anisotropic crystal.[1,2] The SL wave functions, characterized by wave vector $\mathbf{K}$ and band index L, obey Bloch's theorem. Using the envelope-function approach, the $\mathbf{K}=\mathbf{0}$ states of the superlattice are determined as products of envelope functions $F_n(z)$ and the $\mathbf{k}=\mathbf{0}$ Bloch functions $\langle\mathbf{r}|n,0\rangle$ corresponding to band n of the constituent bulk semiconductors:

$$\langle\mathbf{r}|\Psi_{\mathrm{SL}}(L,\mathbf{K}=0)\rangle=\langle\mathbf{r}|L,\mathbf{K}=0\rangle$$

$$=\sum_n F_n(L,\mathbf{K}=0;z)\langle\mathbf{r}|n,0\rangle. \tag{3.1}$$

Here z is the growth direction of the superlattice. The formalism presented applies to any number of bulk bands n. However, we note that in practice it will be restricted to the 14 bands considered in Sec. II.

When the envelope-function expression Eq. (3.1) is substituted into the Hamiltonian [Eq. (2.1)], a multiband effective-mass Hamiltonian is obtained. The wave functions of the bulk states, $\langle\mathbf{r}|n,0\rangle$, are nearly the same in layers A and B due to the similarity in the pseudopotentials and momentum matrix elements for the two materials under consideration.[2,3] The envelope functions are taken to be slowly varying on the scale of the bulk unit-cell size, and can therefore be cell averaged. With these assumptions, the multiband Hamiltonian for $\mathbf{K}=\mathbf{0}$ can be expressed as

$$[H_{A(B)}(k_x,k_y,k_z\rightarrow -i\partial/\partial z)-E_L]\mathbf{F}(L,\mathbf{K}=0;z)=0. \tag{3.2}$$

The envelope functions and energies which are solutions to Eq. (3.2) are labeled by L. The boundary conditions for $\mathbf{F}(L,\mathbf{K}=\mathbf{0};z)$ are obtained by integrating Eq. (3.2) across an interface, and are consistent with continuity of the cell-averaged current,[24]

$$\sum_{n'}\langle n,0|p_z|n',0\rangle F_{n'}(z_+)-\frac{i\hbar}{m}\frac{\partial F_n(z_+)}{\partial z}$$

$$=\sum_{n'}\langle n,0|p_z|n',0\rangle F_{n'}(z_-)-\frac{i\hbar}{m}\frac{\partial F_n(z_-)}{\partial z} \tag{3.3}$$

where $\langle n',0|\mathbf{p}|n,0\rangle$ is the momentum matrix element connecting bulk bands. The bulk momentum-matrix elements of $H_{A(B)}$ contain the effects of the rapidly varying $\langle\mathbf{r}|n,0\rangle$'s.

Once the superlattice $\mathbf{K}=\mathbf{0}$ states have been determined, a superlattice $\mathbf{K}\cdot\mathbf{p}$ theory is used to determine the finite $\mathbf{K}$ states. A finite $\mathbf{K}$ SL state $|L,\mathbf{K}\rangle$ is expressed in terms of the $\mathbf{K}=\mathbf{0}$ states by

$$\langle\mathbf{r}|L,\mathbf{K}\rangle=e^{i\mathbf{K}\cdot\mathbf{r}}\sum_N c_{LN}(\mathbf{K})\langle\mathbf{r}|N,0\rangle$$

$$=e^{i\mathbf{K}\cdot\mathbf{r}}\sum_n F_n(L,\mathbf{K};z)\langle\mathbf{r}|n,0\rangle \tag{3.4}$$

and the Hamiltonian is applied to this state to obtain a SL $\mathbf{K}\cdot\mathbf{p}$ equation for the c_{LN}'s as a function of $\mathbf{K}$:

$$\sum_N\left[\left(E_N(0)+\frac{\hbar^2K^2}{2m}-E_L(\mathbf{K})\right)\delta_{NN'}\right.$$

$$\left.+\langle N',0|H'|N,0\rangle\right]c_{LN'}(\mathbf{K})=0. \tag{3.5}$$

The dispersion of the SL bands is governed by

$$\langle N',0|H'|N,0\rangle=\frac{\hbar\mathbf{K}}{m}\cdot\langle N',0|\mathbf{p}|N,0\rangle, \tag{3.6}$$

where the momentum matrix elements connecting the superlattice $\mathbf{K}=\mathbf{0}$ states are

$$\langle L',0|\mathbf{p}|L,0\rangle=\frac{1}{V}\sum_{nn'}\left\{\left[\int d\mathbf{r}\ F^*_{n'}(L',0;z)F_n(L,0;z)\right]\langle n',0|\mathbf{p}|n,0\rangle+\left[\int d\mathbf{r}\ F^*_{n'}(L',0;z)\mathbf{p}F_n(L,0;z)\right]\delta_{nn'}\right\} \tag{3.7}$$

$$=\sum_{n,n'}[\alpha_{n,n'}(L,L')\langle n',0|\mathbf{p}|n,0\rangle+\Pi_n(L,L')\delta_{n,n'}] \tag{3.8}$$

and V is the crystal volume. The terms involving α are known[2] to be larger by a factor of m/m_C than the terms involving Π. We now adapt the formalism for the effective 8-band model to justify the use of this model in previous calculations of SL interband transitions,[1,3] and to apply it to intersubband transitions in the SL conduction bands.

The folding-down procedure for the SL's is analogous to that presented in detail for bulk bands. The approximations involved in reducing the effective $(8\times8)H_{ps^-}$ are also the same. The superlattice $\mathbf{K}=\mathbf{0}$ states can either be written in the 8-band effective basis or the full 14-band basis,

$$\langle\mathbf{r}|\Psi_{\mathrm{SL}}\rangle=\sum_{n=1}^{8}F_n^{\mathrm{eff}}(L,\mathbf{K}=0;z)\langle\mathbf{r}|n,0\rangle^{\mathrm{eff}} \tag{3.9}$$

$$=\sum_{n=1}^{14}F_n(L,\mathbf{K}=0;z)\langle\mathbf{r}|n,0\rangle. \tag{3.10}$$

The 14-component

$$\mathbf{F}=\begin{bmatrix}\mathbf{F}_{p\bar{s}}\\ \mathbf{F}_{\bar{p}}\end{bmatrix} \tag{3.11}$$

can be expressed for arbitrary $\mathbf{K}$ in terms of the 8-component $\mathbf{F}^{\text{eff}}$ analogously to Eqs. (2.8) and (2.9):

$$\mathbf{F}_{p\bar{s}}(L,\mathbf{K})=\mathbf{F}^{\text{eff}}_{p\bar{s}}(L,\mathbf{K}), \tag{3.12}$$

$$\mathbf{F}_{\bar{p}}(L,\mathbf{K})=-(H_{\bar{p}}-E_L)^{-1}H^{\dagger}_{p\bar{s}\text{-}\bar{p}}\mathbf{F}_{p\bar{s}}(L,\mathbf{K}). \tag{3.13}$$

The essential elements of the procedure are shown schematically in Fig. 1. Equation (3.12) leads to the familiar form for the envelope-function equation

$$[H^{\mathbf{k}\cdot\mathbf{p}}_{A(B)}(k_x,k_y,k_z\rightarrow -i\partial/\partial z)-E]\mathbf{F}_{p\bar{s}}(L,\mathbf{K}=0;z)=0, \tag{3.14}$$

or, explicitly,

$$\begin{pmatrix} E_{\Gamma_6}(z) & \frac{i\hbar Pk_z}{m} & 0 & \frac{i\hbar Pk_z}{\sqrt{2}m}\\ -\frac{i\hbar Pk_z}{m} & E_{\Gamma_8}(z) & 0 & 0\\ 0 & 0 & E_{\Gamma_8}(z)-k_z\frac{\hbar^2}{2m_{\text{HH}}(z)}k_z & 0\\ -\frac{i\hbar Pk_z}{\sqrt{2}m} & 0 & 0 & E_{\Gamma_7}(z)\end{pmatrix}\begin{pmatrix}F_c(z)\\ F_{\text{LH}}(z)\\ F_{\text{HH}}(z)\\ F_{\text{SO}}(z)\end{pmatrix}=E\begin{pmatrix}F_c(z)\\ F_{\text{LH}}(z)\\ F_{\text{HH}}(z)\\ F_{\text{SO}}(z)\end{pmatrix}, \tag{3.15}$$

with $k_z\rightarrow -i(\partial/\partial z)$. The z dependence of matrix elements in $H^{\mathbf{k}\cdot\mathbf{p}}_{A(B)}$ arises because their values differ in the different layers $A(B)$. $E_{\Gamma_n}(z)$ are the energies of the bulk $\mathbf{k}=\mathbf{0}$ states. The values of $m_{\text{HH}}(z)$ can be obtained from Eq. (2.16). They are similarly layer dependent. The heavy-hole mass term originates from $\delta H_{p\bar{s}}$, and is thus a result of folding down the $\bar{p}$ states. Its form

$$\begin{aligned}(\delta H_{p\bar{s}})_{3,3}&=-\left(H_{p\bar{s}\text{-}\bar{p}}\left(\frac{1}{H_{\bar{p}}-E}\right)H^{\dagger}_{p\bar{s}\text{-}\bar{p}}\right)_{3,3}\\ &=\frac{\hbar Qk_z}{m}\left[\frac{1}{2[E-(E_c+E_g)]}+\frac{1}{E-(E_c+E_g-\Delta_c)}\right]\frac{\hbar Qk_z}{m}\end{aligned} \tag{3.16}$$

is thus the same as the empirical expression of Eq. (3.15) used in previous work.

The boundary conditions for the light states (3.3) are

$$\sum_{n'}\langle n,0|p_z|n',0\rangle F_{n'}(z_-)=\sum_{n'}\langle n,0|p_z|n',0\rangle F_{n'}(z_+), \tag{3.17}$$

where $\langle n',0|p_z|n,0\rangle$ are the momentum-matrix elements among the bulk bands given explicitly by Eq. (B2) in Appendix B. The Π terms in the SL momentum matrix elements [Eq. (3.8)] are neglected.

Due to the folding down of the $\bar{p}$ states, the boundary conditions for the heavy-hole $\mathbf{K}=0$ states take another form,

$$\begin{aligned}&\left[1-\frac{Q^2[3E_c(z_+)+3E_g(z_+)-\Delta_c(z_+)]}{m[E_c(z_+)+E_g(z_+)][E_c(z_+)+E_g(z_+)-\Delta_c(z_+)]}\right]\frac{\partial F_{\text{HH}}(z_+)}{\partial z}\\ &\quad=\left[1-\frac{Q^2[3E_c(z_-)+3E_g(z_-)-\Delta_c(z_-)]}{m[E_c(z_-)+E_g(z_-)][E_c(z_-)+E_g(z_-)-\Delta_c(z_-)]}\right]\frac{\partial F_{\text{HH}}(z_-)}{\partial z}.\end{aligned} \tag{3.18}$$

This justifies the use of the boundary conditions in Ref. 2,

$$F_{\text{HH}}(z_+)=F_{\text{HH}}(z_-)\quad\text{and}\quad\frac{1}{m_{\text{HH}}(z_+)}\frac{\partial F_{\text{HH}}(z_+)}{\partial z}=\frac{1}{m_{\text{HH}}(z_-)}\frac{\partial F_{\text{HH}}(z_-)}{\partial z}. \tag{3.19}$$

The heavy-hole mass m_{HH} can be determined for a bulk constituent within the 14-band model from the zone-center band gaps and Q according to Eq. (2.16). In our 14-band semiempirical parametrization, Q is chosen to reproduce the experimental value of m_{HH}, while in the 8-band parametrization the experimental value of m_{HH} is used directly.

The matrix elements coupling heavy-hole superlattice bands along K_z differ from those of Eq. (3.6). There are three types of terms coupling the heavy-hole bands along the K_z direction. These are given by

$$\langle N',0|H_z'|N,0\rangle = -\frac{\hbar^2 K_z}{2iV}\int d\mathbf{r}\, F^*_{\mathrm{HH}}(N',0;\mathbf{r})\left[\frac{\partial}{\partial z}\frac{1}{m_{\mathrm{HH}}(z)}\right]F_{\mathrm{HH}}(N,0;\mathbf{r}) - \frac{\hbar^2 K_z^2}{2V}\int d\mathbf{r}\, F^*_{\mathrm{HH}}(N',0;\mathbf{r})\left[\frac{1}{m_{\mathrm{HH}}(z)}\right]F_{\mathrm{HH}}(N,0;\mathbf{r}) - \frac{\hbar^2 K_z}{iV}\int d\mathbf{r} F^*_{\mathrm{HH}}(N',0;\mathbf{r})\left[\frac{1}{m_{\mathrm{HH}}(z)}\frac{\partial}{\partial z}\right]F_{\mathrm{HH}}(N,0;\mathbf{r}). \tag{3.20}$$

The first term contributes only at the interfaces, where $m_{\mathrm{HH}}(z)$ may be discontinuous. The second term is proportional to the overlap of the envelope functions. The third term involves an envelope-function derivative and is similar to a Π term.

Having now specified the form of all the matrix elements in the SL $\mathbf{K}\cdot\mathbf{p}$ secular equation [Eq. (3.5)], it is now possible to solve this equation for arbitrary $\mathbf{K}$ to obtain accurate nonparabolic band structures. Once the SL energies $E_L(\mathbf{K})$ and envelope functions $\mathbf{F}_{ps^-}(L,\mathbf{K};z)$ have been found, the p envelope functions $\mathbf{F}_{p^-}(L,\mathbf{K};z)$ are determined by (3.13).

In addition to the bulk parameters described in Sec. II, the empirical valence-band offset $\Lambda = E_{\Gamma_8}(A) - E_{\Gamma_8}(B)$ and the layer thicknesses provide the remaining necessary information to calculate the band structure of the superlattice. Table III shows these parameters for the semiconductor systems analyzed in this paper. The valence-band offset is affected by strain,[8] and differs for the heavy and light holes:

$$\Lambda_{\mathrm{HH}} = \Lambda + e_B^A b^A - e_B^B b^B, \tag{3.21}$$

$$\Lambda_{\mathrm{LH}} = \Lambda - e_B^A b^A + e_B^B b^B + \frac{2(e_B^A b^A)^2}{\Delta^A} - \frac{2(e_B^B b^B)^2}{\Delta^B}.$$

The $\mathbf{K}=0$ Hamiltonian can be made block diagonal as a result of the parity symmetry of the 8-band model. This symmetry remains in the superlattice for general $\mathbf{K}$, but was not utilized in the formalism of Ref. 2, in which the 8-band effective Hamiltonian only decomposed into two 4×4 blocks at $\mathbf{K}_\parallel=\mathbf{0}$ because the matrices $\langle n',0|p_x|n,0\rangle$ [Eq. (B3)] and $\langle n',0|p_y|n,0\rangle$ are not block diagonal. p_{x,ps^-} can be rendered block diagonal through a judicious choice of basis states. The appropriate conduction band states, for example, are[3]

$$|1'\rangle = (|1\rangle + |5\rangle)/\sqrt{2}, \qquad |5'\rangle = (|1\rangle - |5\rangle)/\sqrt{2}. \tag{3.22}$$

The block diagonalization of p_{x,ps^-} into two (4×4) matrices reduces the computational requirements by a factor of 8.

Twenty SL $\mathbf{K}=\mathbf{0}$ bands (forty spin-dependent bands) are kept for the SL $\mathbf{K}\cdot\mathbf{p}$ calculation: the five closest to the fundamental gap whose characters are C, LH, HH, and SO. These are not necessarily the highest 15 valence bands, but are chosen to balance the truncated basis set to improve convergence of the $\mathbf{K}\cdot\mathbf{p}$ theory.

The above formalism is a highly optimized adaptation of work begun in Ref. 2. The band structure and optical absorption (including excitons) can be calculated for a superlattice in 5 min of CPU time on a desktop workstation. The optical-absorption calculations agree with experiment to within 10% for III-V systems.[5] Auger lifetimes, relevant to IR detectors and lasers, which are calculated using these band structures agree with measurements within experimental error.[25]

TABLE III. Empirical $\mathbf{K}\cdot\mathbf{p}$ parameters required (along with those in Table II) for the calculations of Sec. IV. Values for E_g at 300 K are used. All values are from Ref. 23 except Λ, which comes from Ref. 31. The barrier composition of Ref. 11, $Al_{0.31}Ga_{0.69}As$, has identical parameters to $Al_{0.3}Ga_{0.7}As$ with the exception of a slightly different E_g (1.799 eV).

	GaAs	$Al_{0.3}Ga_{0.7}As$	GaAs/$Al_{0.3}Ga_{0.7}As$
E_g energy gap (eV)	1.420	1.786	
Δ spin-orbit splitting (eV)		0.328	
m^*_{HH} in (100) direction		0.48	
Λ valence-band offset (eV)			0.138
n_0 index of refraction			3.5

IV. INTERSUBBAND ABSORPTION FROM CRYSTAL SUPERLATTICE K·p THEORY

The momentum-matrix elements involving p_z and p_x determine both the effective masses and the optical absorption along or perpendicular to the growth axis, respectively. Johnson *et al.*[1] used the f-sum rule

$$(m/m_L)_\alpha = 1 + \sum_{L'}{}' f^\alpha_{L'L} \tag{4.1}$$

to show that the 50% difference between the $C1$ effective masses m^z_{C1} and m^x_{C1} is almost entirely associated with the fact that $f^z_{C2,C1} \gg f^x_{C2,C1}$ for a particular GaAs/$Al_xGa_{1-x}As$ SL. Here

$$f^\alpha_{L'L} = \frac{2}{m}\frac{|\langle L,0|p_\alpha|L',0\rangle|^2}{E_L(0)-E_{L'}(0)} \tag{4.2}$$

is the oscillator strength, $\alpha = z$ or x and L, L' are SL subband indices, and the prime on the summation indicates that $L' = L$ is excluded. The calculated values were shown to be in agreement with experimental cyclotron resonance values.[14] This fact leads to the conclusion, in agreement with the present calculations for both 8- and 14-band models, that the $C1 \rightarrow C2$ intersubband TM absorption determined by p_z

is considerably larger than the corresponding absorption, determined by p_x, for the TE mode.

Recently Peng and Fonstad[17] have argued that the TE absorption calculated in a 14-band model was dramatically larger than the small TE absorption originating from the spin-orbit interaction in an 8-band model. They also identified the source of the strong TE absorption to be P_1 and Q, defined in Eq. (2.2), which appears in the 14-band model. The TE absorption in the 14-band model is indeed larger by a factor of 100–1000, but it remains 5–10 times smaller than the TM absorption and therefore relatively insignificant.

This section begins with a brief summary of the formal intersubband absorption results using the 14-band model, and then discusses quantitative results for the above-mentioned systems of experimental interest (see Sec. I).

A. Formalism

The expressions for TM and TE intersubband absorption in SL notation are

$$\alpha_{x(z)}(\omega)=\frac{2\pi^2e^2}{m^2c\omega V}\sum_{\mathbf{K}}\sum_{L,L'}\{f_n[E_{L'}(\mathbf{K})]-f_n[E_L(\mathbf{K})]\}|\langle L,\mathbf{K}|p_{x(z)}|L',\mathbf{K}\rangle|^2\times\delta[E_L(\mathbf{K})-E'_L(\mathbf{K})-\hbar\omega]. \tag{4.3}$$

As seen graphically in Fig. 3, the changes in the energies of the superlattice bands due to inclusion of the $\bar{p}$ states are small. Therefore the primary change in α_x and α_z due to the $\bar{p}$ states will result from changes in $\langle L,\mathbf{K}|p_x|L',\mathbf{K}\rangle$ and $\langle L,\mathbf{K}|p_z|L,'\mathbf{K}\rangle$. We now consider the effect of the conduction p states on these superlattice matrix elements. The matrices containing $\langle n',0|p_x|n,0\rangle$ and $\langle n',0|p_z|n,0\rangle$ in the 14-band bulk basis decompose into an 8×8 $\mathbf{p}_{x(z),p\bar{s}}$, 8×6 matrix $\mathbf{p}_{x(z),p\bar{s}\text{-}\bar{p}}$, and a 6×6 matrix $\mathbf{p}_{x(z),\bar{p}}$, [$\mathbf{p}_{x(z),\bar{p}}=\mathbf{0}$.]

Using Eq. (3.10), the TE and TM matrix elements can be written in the form

$$\langle L,\mathbf{K}|p_{x(z)}|L',\mathbf{K}\rangle=\mathbf{F}^{\dagger}(L,\mathbf{K})\mathbf{p}_{x(z)}\mathbf{F}(L',\mathbf{K})=\mathbf{F}^{\dagger}_{ps}(L,\mathbf{K})\mathbf{p}_{x(z),p\bar{s}}\mathbf{F}_{p\bar{s}}(L',\mathbf{K}) \tag{4.4}$$

$$+\mathbf{F}^{\dagger}_{ps}(L,\mathbf{K})\mathbf{p}^{\dagger}_{x(z),p\bar{s}\text{-}\bar{p}}\mathbf{F}_{\bar{p}}(L',\mathbf{K})+\mathbf{F}^{\dagger}_{\bar{p}}(L,\mathbf{K})\mathbf{p}_{x(z),p\bar{s}\text{-}\bar{p}}\mathbf{F}_{p\bar{s}}(L',\mathbf{K}). \tag{4.5}$$

The first term (4.4) is that calculated within the 8-band model. The next two terms (4.5) are the first-order additional contributions of the 14-band model.

B. Results

This section will illustrate the intersubband absorption of three GaAs/Al_xGa_{1-x}As quantum-well SL systems using the present theoretical results. The first two cases deal with $C1\rightarrow C2$ transitions originally studied in connection with CALM.[13,26] The third case involves the $C1\rightarrow\Sigma_nCn$ intersubband transitions involved in QWIP applications.[11] The

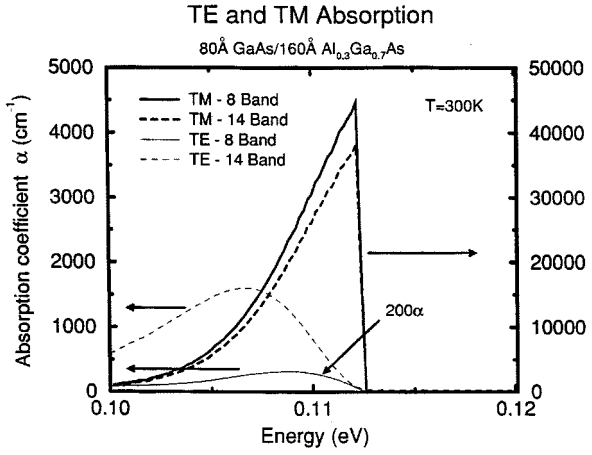

FIG. 4. Absorption for a CALM candidate, in the TE and TM modes, calculated with 8- and 14-band models. 200α indicates that the 8-band TE curve is shown 200 times larger than reality.

$\mathbf{K}\cdot\mathbf{p}$ parameters are given in Table III. The first case considers a 80-Å GaAs/160-Å $Al_{0.3}Ga_{0.7}As$ SL with doping $n=5\times10^{17}$ cm^{-3} in which $C1$ and $C2$ are both localized in the well. The optical-absorption coefficients $\alpha(E)$ at $T=300$ K for photons having TM and TE polarizations are shown in Fig. 4 for both 8- and 14-band models. (The optical length for this and other absorption results in this paper includes the entire SL period.) The large maximum absorption coefficient and the narrowness of the structure for the TM mode is associated with the nesting of the $C1$ and $C2$ subbands: the in-plane masses differ by less than 10%. Since the $C2$ mass is larger than that of $C1$, the range for which $\alpha(E)$ is nonvanishing lies between the diffuse subband energy gap in the vicinity of the Fermi energy $E_g^{C2,C1}(K_F)$ and the sharp energy associated with the maximum value at $K=0$, $E_g^{C2,C1}(0)$, an interval of only about 0.01 eV (cf. Ref. 26, Fig. 4). The sharp feature is absent in the TE case because the optical matrix elements increase with the SL momentum, as pointed out in Ref. 27. As a result, the TE absorption matrix occurs at a lower energy than the sharp TM peak.

The difference between the 8- and 14-band models for the TM case are seen to be small, about 15%, corresponding to a momentum-matrix element difference of 7%. By contrast, the TE absorption for the former is about 10^3 greater than that for the latter. The large difference is due mainly to the incorporation of P_1 and Q [Eq. (2.2)] in the 14-band model, as first pointed out, to our knowledge, by Peng and Fonstad.[17]

Because the result is independent of broadening, the comparison between absorption strengths is better made by using

the conductivity sum rule[28] applied to the narrow absorption band associated with the $C1 \rightarrow C2$ transition. The imaginary part $\delta\epsilon_2^{C2,C1}[x(z);\omega]$ of the dielectric function associated with TE(x) and TM(z) photon polarizations, respectively, is given by Eq. (20) of Ref. 2:

$$\delta\epsilon_2^{C2,C1}[x(z);\omega]=\frac{4\pi^2e^2}{m^2\omega^2}|\langle C1,0|p_{x(z)}|C2,0\rangle|^2\rho_{C2,C1}(\omega), \tag{4.6}$$

where $\rho_{C2,C1}(\omega)$ is the joint density of states per unit energy and volume involving $C1$ and $C2$ bands, and ω is confined to the region $E_g^{C2,C1}(K_{11}=K_F)<\hbar\omega<E_g^{C2,C1}(0)$ having width $n/\rho_{C2,C1}(\omega)$; $\delta\epsilon_2=0$ otherwise. Since the carrier density n is confined to a narrow region around $K=0$ of the $C1$ band, it is sufficient to approximate the momentum-matrix element by its $K=0$ value. The conductivity sum rule then reads

$$\int_0^\infty \omega\,\delta\epsilon_2^{C2,C1}[x(z);\omega]d\omega=-\frac{2\pi^2e^2n}{m}f_{C2,C1}^{x(z)}, \tag{4.7}$$

where $f_{C2,C1}^{x(z)}$ is given by Eq. (4.2). For the TM case, Eq. (4.7) takes the more familiar but approximate form

$$\int_0^\infty \omega\,\delta\epsilon_2^{C2,C1}(z;\omega)d\omega\approx\frac{1}{2}\pi\omega_p^{*2}, \tag{4.8}$$

where $\omega_p^{*2}=4\pi ne^2/m_{C1}^x$ expresses the effective plasma frequency squared in terms of n, and the in-plane effective mass m_{C1}^x. Equation (4.8) is applicable because the sharp feature shown in Fig. 4 is well separated from that of higher conduction subbands. We shall denote the integral having the form in Eq. (4.7) as $\mathscr{A}_{Cn,C1}^{x(z)}$ to denote the transitions $C1\rightarrow Cn$ for the TE(x) or TM(z) mode. The relative absorption strength (RAS) of TE/TM is then given in the present case by the ratio

$$\begin{aligned}\mathscr{A}_{C2,C1}^x/\mathscr{A}_{C2,C1}^z&=|\langle C1,0|p_x|C2,0\rangle|^2/|\langle C1,0|p_z|C2,0\rangle|^2\\&=f_{C2,C1}^x/f_{C2,C1}^z.\end{aligned} \tag{4.9}$$

RAS is 10^{-4} and 0.096 for the 8- and 14-band models, respectively; i.e., the TE absorption is enhanced by a factor of 860.

In a narrower well the absorption features are broader. The increased confinement raises the energies of the Cn levels. Figure 5 shows the absorption for a 40-Å GaAs/200-Å $Al_{0.3}Ga_{0.7}As$ SL with the same doping as in Fig. 4. The two peaks correspond to the $C2$ and $C3$ subbands, which lie close together near the top of the barrier. The nesting between the $C1$ and $C2$ subbands has largely disappeared; hence $\alpha(E)$ is much smaller. The right-hand side of Eq. (4.7) must be generalized to read $(-2\pi^2e^2n/m)\Sigma_n' f_{Cn,C1}^{x(z)}$. The dominant contributions are given by $2\leqslant n\leqslant 5$. Note that since the carrier density n is entirely associated with the $C1$ subband, the value of ω_p^{*2} is unchanged for the TM mode. As a result the TM total absorption strength is the same as in Fig. 4. The numerical calculations verify this observation. The 8- and 14-band TM results still differ little. The relative absorption strength (RAS) is now given formally by

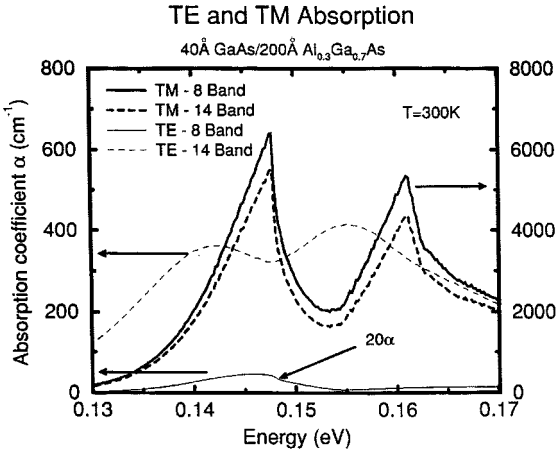

FIG. 5. Absorption for a less-favorable CALM candidate, in the TE and TM modes, calculated with the 8- and 14-band models. 20α indicates that the eight-band TE curve is shown 20 times larger than reality.

$$\begin{aligned}\mathrm{RAS}&=\left[\sum_n{}' \mathscr{A}_{Cn,C1}^x \Big/ \sum_n{}' \mathscr{A}_{Cn,C1}^z\right]\\&=\left[\sum_n{}' f_{Cn,C1}^x \Big/ \sum_n{}' f_{Cn,C1}^z\right],\end{aligned} \tag{4.10}$$

and is calculated for $2\leqslant n\leqslant 5$. The values are 3×10^{-4} and 0.13, respectively, for the 8- and 14-band models due to the effect of P_1 and Q in the latter case. Despite this enhancement, the TE absorption still remains at 13% of the TM value.

The final case to be considered in detail is a QWIP candidate, 40-Å GaAs/300-Å $Al_{0.31}Ga_{0.69}As$, which is n doped with 2.4×10^{17}-cm^{-3} carriers.[11] Figure 6(a) shows the TM absorption measured for this system, and that calculated in the 8- and 14-band models. The data for the absolute absorption coefficient in Ref. 11 are for the TM mode. According to Ref. 12, they are obtained using a waveguide geometry and the assumption that there is no TE contribution. The calculated curves have been broadened by 20 meV to account for plausible ±1 layer uncertainties in the SL well width used successfully in previous calculations by the present group (e.g., Ref. 5). The quantitative agreement between the 14-band calculation and experiment is seen to be satisfactory. (Perfect agreement could be obtained by making small changes in the broadening, doping, or alloy concentration.) The 8- and 14-band absorptions differ by 17%, indicating a difference in the momentum-matrix elements of 8%.

Figure 6(b) shows the calculated TE absorption and TM absorption coefficients for the 14-band model to emphasize that the TE process is appreciable but not as large as that predicted by Peng's theory[17] or some recent experiments.[15,16] The Cn states $2\leqslant n\leqslant 5$ summed over in Eq. (4.10) all lie in the continuum. The contribution to RAS for $n>5$ is small. The values of RAS for the 8- and 14-band models are 1.6×10^{-3} and 0.19 respectively. Thus, as shown in Fig. 6(b), the TE absorption strength is 20% of that due to TM and is observable as suggested in Ref. 17. However, as pointed out at the beginning of this section, the two absorption peaks cannot have equal values because of the f-sum rule (4.2) and

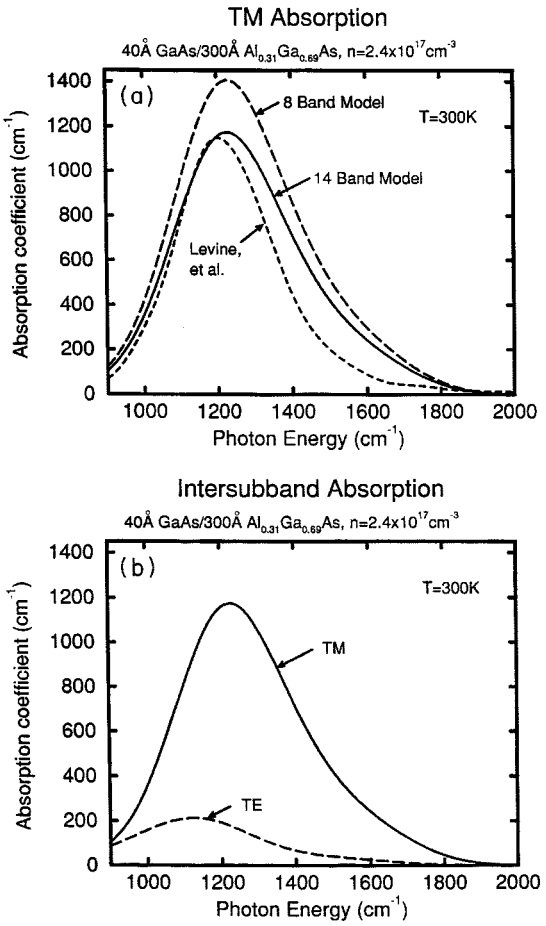

FIG. 6. (a) TM absorption for a QWIP candidate studied by Levine *et al.* (Ref. 11), calculated with 8- and 14-band models, and compared to experiment. (b) TE absorption compared to TM absorption for the same system in the 14-band model.

the fact that the principal axis values of the effective masses m_{C1}^{x} and m_{C1}^{z} must differ in the anisotropic solid represented by the SL.

The observation that the TE/TM relative absorption can be sufficiently large to be seen experimentally in narrow GaAs QW's having a width of about 40 Å is noteworthy. This result comes about because the $C1$ state is confined within the QW, and the excited bands Cn $(n \geqslant 2)$ lie in the continuum. Furthermore, there are several $(2 \leqslant n \leqslant 5)$ bands that contribute in the same relatively narrow energy range enhancing the absorption [cf. Figs. 6(a) and (b)]. Equation (4.9) indicates that the smaller RAS associated with the results of Fig. 4 relative to those of Fig. 6(b) is due to the smaller *relative* value of the momentum-matrix elements connecting $C1$ to another bound state ($C2$ in Fig. 4) relative to those involving continuum final states ($C2$ to $C5$ in Fig. 6). Evidently the QW's on QWIP's cannot be too narrow since $C1$ must be bound in the well to prevent conduction along the growth direction. The barriers cannot be made too thin for the same reason. In addition, each well should provide sufficiently large optical absorption to minimize the number of required SL layers.

Finally we note that the large numerical estimate in Ref. 17 was based on the assumption that $\|\Psi_{\bar{p}}\| \sim \|\Psi_{p\bar{s}}\|$. The inaccuracy of this estimate has been explored in Ref. 18. Our calculations indicate that the experiments reporting large TE/TM absorption ratios involving 44-Å $In_xGa_{1-x}As$/250-Å GaAs (Ref. 15) and 18-Å $In_xGa_{1-x}As$/50-Å AlAs (Ref. 16) have RAS values of 2.5% and 0.7%, respectively. The physical effects identified as responsible for the large TE/TM ratios in Ref. 15 are incorrectly attributed to ingredients of the eight-band model. An evaluation of the effectiveness of surface roughness in inducing diffuse reflection and therefore affecting the TE/TM ratio indicates that its influence would be negligible.[29] Large TE/TM absorption ratios have also been observed in systems having an applied electric field along the growth direction.[30] These effects on the momentum matrix elements will be examined in a future paper.

We conclude that TE absorption should be observable in narrow GaAs QW systems. However, on the basis of the f-sum rule resulting in $C1$ band mass anisotropies observed by cyclotron resonance experiments and the conductivity sum rule describing the well-isolated optical frequency range in which $C1 \rightarrow Cn$ transitions occur, the limiting TE absorption is estimated to be no larger than about 20% of that associated with the TM mode. The significance of TE absorption on normal-incidence QWIP applications remains doubtful.

ACKNOWLEDGMENTS

We are grateful for helpful discussions and comments from R. V. Jones, E. Runge, and M. Z. Tidrow. This work was supported by the U.S. Advanced Research Projects Agency (ARPA) through the U.S. Office of Naval Research (ONR) Contract No. N00014-93-1-0549 and by an ARPA/URI subcontract through Brown University No. 283-250040.

APPENDIX A: BULK EQUATIONS

The 14 bulk $\mathbf{k}=\mathbf{0}$ basis states $\langle \mathbf{r}|n,0\rangle$ being considered are defined in Table I. The first eight, the $p\bar{s}$ states, are defined in terms of the states $|S\rangle$, $|X\rangle$, $|Y\rangle$, and $|Z\rangle$ using the notation of Ref. 2. The $\bar{p}$ states are defined in terms of the states $|X^c\rangle$, $|Y^c\rangle$, and $|Z^c\rangle$ using the notation in Ref. 22.

It is possible to write the 8×8 $H_{p\bar{s}}$ in block-diagonal form,

$$H_{p\bar{s}}=\begin{bmatrix} h_{p\bar{s}} & 0 \\ 0 & h_{p\bar{s}} \end{bmatrix}, \tag{A1}$$

where

$$h_{p\bar{s}}=\frac{\hbar^2k^2}{2m}+\begin{bmatrix} E_g & \frac{iP_0\hbar k}{m} & 0 & \frac{iP_0\hbar k}{\sqrt{2}m} \\ -\frac{iP_0\hbar k}{m} & 0 & 0 & 0 \\ 0 & 0 & 0 & 0 \\ -\frac{iP_0\hbar k}{\sqrt{2}m} & 0 & 0 & -\Delta \end{bmatrix}. \tag{A2}$$

$H_{p\bar{s}\text{-}\bar{p}}$ can be similarly decomposed:

$$H_{p\bar{s}\text{-}\bar{p}}=\begin{bmatrix} h_{p\bar{s}\text{-}\bar{p}} & 0 \\ 0 & h_{p\bar{s}\text{-}\bar{p}} \end{bmatrix}, \tag{A3}$$

where

$$h_{p\bar{s}-\bar{p}}=\begin{bmatrix} \frac{iP_1\hbar k}{m} & 0 & \frac{iP_1\hbar k}{\sqrt{2}m} \\ 0 & -\frac{Q\hbar k}{\sqrt{2}m} & 0 \\ \frac{Q\hbar k}{\sqrt{2}m} & 0 & -\frac{Q\hbar k}{m} \\ 0 & \frac{Q\hbar k}{m} & 0 \end{bmatrix}. \tag{A4}$$

Finally, $H_{\bar{p}}$ is diagonal, and

$$h_{\bar{p}}=\begin{bmatrix} E_c+E_g & 0 & 0 \\ 0 & E_c+E_g & 0 \\ 0 & 0 & E_c+E_g-\Delta_c \end{bmatrix}. \tag{A5}$$

The resultant $H_{p\bar{s}}^{\text{eff}}$ is block diagonal, like Eq. (A1), and

$$h_{p\bar{s}}^{\text{eff}}=h_{p\bar{s}}+\delta h_{p\bar{s}},$$

where

$$\delta h_{p\bar{s}}=\frac{\hbar^2k^2}{2m}\begin{pmatrix} \frac{P_1^2}{m}\left[\frac{2}{E-(E_c+E_g)}+\frac{1}{E-(E_c+E_g-\Delta_c)}\right] & 0 & \frac{iP_1Q}{m}\left[\frac{\sqrt{2}}{E-(E_c+E_g)}-\frac{\sqrt{2}}{E-(E_c+E_g-\Delta_c)}\right] & 0 \\ 0 & \frac{Q^2}{m[E-(E_c+E_g)]} & 0 & -\frac{\sqrt{2}Q^2}{m[E-(E_c+E_g)]} \\ -\frac{iP_1Q}{m}\left[\frac{\sqrt{2}}{E-(E_c+E_g)}-\frac{\sqrt{2}}{E-(E_c+E_g-\Delta_c)}\right] & 0 & \frac{Q^2}{m}\left[\frac{1}{E-(E_c+E_g)}+\frac{2}{E-(E_c+E_g-\Delta_c)}\right] & 0 \\ 0 & -\frac{\sqrt{2}Q^2}{m[E-(E_c+E_g)]} & 0 & \frac{Q^2}{m[E-(E_c+E_g)]} \end{pmatrix}. \tag{A6}$$

When the free-electron mass has been neglected, and all features of $\delta h_{p\bar{s}}$ except the induced heavy-hole mass term are neglected, as discussed in Sec. I, $h_{p\bar{s}}^{\text{eff}}$ reduces to $h^{\mathbf{k}\cdot\mathbf{p}}$, where

$$h^{\mathbf{k}\cdot\mathbf{p}}=\begin{pmatrix} E_g & \frac{iP_0\hbar k}{m} & 0 & \frac{iP_0\hbar k}{\sqrt{2}m} \\ -\frac{iP_0\hbar k}{m} & 0 & 0 & 0 \\ 0 & 0 & -\frac{\hbar^2k^2}{2m_{\text{HH}}} & 0 \\ -\frac{iP_0\hbar k}{\sqrt{2}m} & 0 & 0 & -\Delta \end{pmatrix}. \tag{A7}$$

The heavy-hole mass comes from the (3,3) element of Eq. (A6), and is

$$\frac{m}{m_{\mathrm{HH}}}=1-\frac{Q^2(3E_c+3E_g-\Delta_c)}{m(E_c+E_g)(E_c+E_g-\Delta_c)}. \tag{A8}$$

APPENDIX B: SUPERLATTICE EQUATIONS

The effective 8-band bulk Hamiltonian $H^{\mathbf{k}\cdot\mathbf{p}}$ [Eq. (A7)] forms the basis for the envelope-function formalism used to obtain the SL electronic structure. The bulk constituents of the two layers of the superlattice have different zone-center bulk band energies. Therefore the zone-center energies become position dependent in the resulting multiband effective Hamiltonian. Because of the dependence of m_{HH} on bulk band energies [Eq. (A8)], the heavy-hole mass is also position dependent. The offset between the two sets of band energies also must be known. The Schrödinger equation with this Hamiltonian is

$$\begin{pmatrix} E_{\Gamma_6}(z) & \frac{i\hbar Pk_z}{m} & 0 & \frac{i\hbar Pk_z}{\sqrt{2}m} \\ -\frac{i\hbar Pk_z}{m} & E_{\Gamma_8}(z) & 0 & 0 \\ 0 & 0 & E_{\Gamma_8}(z)-k_z\frac{\hbar^2}{2m_{\mathrm{HH}}(z)}k_z & 0 \\ -\frac{i\hbar Pk_z}{\sqrt{2}m} & 0 & 0 & E_{\Gamma_7}(z) \end{pmatrix} \begin{pmatrix} F_c(z) \\ F_{\mathrm{LH}}(z) \\ F_{\mathrm{HH}}(z) \\ F_{\mathrm{SO}}(z) \end{pmatrix} = E \begin{pmatrix} F_c(z) \\ F_{\mathrm{LH}}(z) \\ F_{\mathrm{HH}}(z) \\ F_{\mathrm{SO}}(z) \end{pmatrix}, \tag{B1}$$

with $k_z \rightarrow -i(\partial/\partial z)$. Quantities in the Hamiltonian which are z dependent merely depend on the layer that z is in, which is why the Hamiltonian is designated $H^{\mathbf{k}\cdot\mathbf{p}}_{A(B)}$. $E_{\Gamma_m}(z)$ are the energies of the bulk $\mathbf{k}=\mathbf{0}$ states. The form $k_z[\hbar^2/m_{\mathrm{HH}}(z)]k_z$ for the heavy-hole mass term in the Hamiltonian is due to the folding-down procedure, where $\delta H_{p\bar{s}}=-H_{p\bar{s}\text{-}\bar{p}}(H_{\bar{p}}-E)^{-1}H^{\dagger}_{p\bar{s}\text{-}\bar{p}}$. Since $H_{p\bar{s}\text{-}\bar{p}}$ is proportional to k, and $(H_{\bar{p}}-E)^{-1}$ has position-dependent energy denominators, the correct form for the heavy-hole term is that in Eq. (B1).

The effect of strain is to change the zone-center energies of the bands (the diagonal elements of $H_{A(B)}$), so there is no effect on the structure of the derivation we have presented. Since strain does not affect the momentum-matrix elements of the bulk crystals, it enters only into the determination of the $\mathbf{K}=\mathbf{0}$ states. The derivation for the SL electronic structure can be considered to include strain from the beginning.

The momentum-matrix elements among the 14 bulk bands can be broken down into an 8×8 matrix $\mathbf{p}_{p\bar{s}}$, an 8×6 matrix $\mathbf{p}_{p\bar{s}\text{-}\bar{p}}$, and a 6×6 matrix $\mathbf{p}_{\bar{p}}$ ($\mathbf{p}_{\bar{p}}=0$). The boundary conditions [Eq. (3.17)] on the multiband Hamiltonian Eq. (B1) require knowledge of

$$\mathbf{p}_{z,p\bar{s}}=\begin{pmatrix} 0 & iP_0 & 0 & \frac{iP_0}{\sqrt{2}} & 0 & 0 & 0 & 0 \\ -iP_0 & 0 & 0 & 0 & 0 & 0 & 0 & 0 \\ 0 & 0 & 0 & 0 & 0 & 0 & 0 & 0 \\ -\frac{iP_0}{\sqrt{2}} & 0 & 0 & 0 & 0 & 0 & 0 & 0 \\ 0 & 0 & 0 & 0 & 0 & iP_0 & 0 & \frac{iP_0}{\sqrt{2}} \\ 0 & 0 & 0 & 0 & -iP_0 & 0 & 0 & 0 \\ 0 & 0 & 0 & 0 & 0 & 0 & 0 & 0 \\ 0 & 0 & 0 & 0 & -\frac{iP_0}{\sqrt{2}} & 0 & 0 & 0 \end{pmatrix}. \tag{B2}$$

For the SL $\mathbf{K}\cdot\mathbf{p}$ equation [Eq. (3.5)]

$$\mathbf{p}_{x,p\bar{s}}=\begin{pmatrix} 0 & 0 & 0 & 0 & 0 & \frac{iP_0}{2} & \frac{i\sqrt{3}P_0}{2} & -\frac{iP_0}{\sqrt{2}} \\ 0 & 0 & 0 & 0 & \frac{iP_0}{2} & 0 & 0 & 0 \\ 0 & 0 & 0 & 0 & -\frac{i\sqrt{3}P_0}{2} & 0 & 0 & 0 \\ 0 & 0 & 0 & 0 & -\frac{iP_0}{\sqrt{2}} & 0 & 0 & 0 \\ 0 & -\frac{iP_0}{2} & \frac{i\sqrt{3}P_0}{2} & \frac{iP_0}{\sqrt{2}} & 0 & 0 & 0 & 0 \\ -\frac{iP_0}{2} & 0 & 0 & 0 & 0 & 0 & 0 & 0 \\ -\frac{i\sqrt{3}P_0}{2} & 0 & 0 & 0 & 0 & 0 & 0 & 0 \\ \frac{iP_0}{\sqrt{2}} & 0 & 0 & 0 & 0 & 0 & 0 & 0 \end{pmatrix}$$

is also necessary. In the choice of basis sets described in Sec. III, $\mathbf{p}_{x,p\bar{s}}$ is block diagonal. $\mathbf{p}_{p\bar{s}\text{-}\bar{p}}$ is required for determining the momentum-matrix elements [Eq. (4.5)]

$$\mathbf{p}_{z,p\bar{s}-\bar{p}}=\begin{pmatrix} iP_1 & 0 & \frac{iP_1}{\sqrt{2}} & 0 & 0 & 0 \\ 0 & -\frac{Q}{\sqrt{2}} & 0 & 0 & 0 & 0 \\ \frac{Q}{\sqrt{2}} & 0 & -Q & 0 & 0 & 0 \\ 0 & Q & 0 & 0 & 0 & 0 \\ 0 & 0 & 0 & iP_1 & 0 & \frac{iP_1}{\sqrt{2}} \\ 0 & 0 & 0 & 0 & -\frac{Q}{\sqrt{2}} & 0 \\ 0 & 0 & 0 & \frac{Q}{\sqrt{2}} & 0 & -Q \\ 0 & 0 & 0 & 0 & Q & 0 \end{pmatrix}$$

and

$$\mathbf{p}_{x,p\bar{s}-\bar{p}}=\begin{pmatrix} 0 & 0 & 0 & \frac{iP_1}{2} & \frac{i\sqrt{3}P_1}{2} & -\frac{iP_1}{\sqrt{2}} \\ 0 & 0 & 0 & 0 & -\frac{Q}{\sqrt{2}} & -\frac{\sqrt{3}Q}{2} \\ 0 & 0 & 0 & -\frac{Q}{\sqrt{2}} & 0 & -\frac{Q}{2} \\ 0 & 0 & 0 & \frac{\sqrt{3}Q}{2} & -\frac{Q}{2} & 0 \\ -\frac{iP_1}{2} & \frac{i\sqrt{3}P_1}{2} & \frac{iP_1}{\sqrt{2}} & 0 & 0 & 0 \\ 0 & \frac{Q}{\sqrt{2}} & -\frac{\sqrt{3}Q}{2} & 0 & 0 & 0 \\ \frac{Q}{\sqrt{2}} & 0 & \frac{Q}{2} & 0 & 0 & 0 \\ \frac{\sqrt{3}Q}{2} & \frac{Q}{2} & 0 & 0 & 0 & 0 \end{pmatrix}$$

*Present address: Department of Physics and Astronomy, University of Iowa, Iowa City, IA 52242.

†Author to whom all correspondence should be addressed.

[1] N. F. Johnson, H. Ehrenreich, K. C. Hass, and T. C. McGill, Phys. Rev. Lett. **59**, 2352 (1987).

[2] N. F. Johnson, H. Ehrenreich, P. M. Hui, and P. M. Young, Phys. Rev. B **41**, 3655 (1990).

[3] P. M. Young, Ph.D. thesis, Harvard University, 1992.

[4] For a review, see G. Bastard, J.-A. Brum, and R. Ferreira, in *Solid State Physics*, edited by H. Ehrenreich and D. Turnbull (Academic, Boston, 1991), Vol. 44, p. 229.

[5] P. M. Young, P. M. Hui, and H. Ehrenreich, Phys. Rev. B **44**, 12 969 (1991).

[6] P. M. Young, H. Ehrenreich, P. M. Hui, and N. F. Johnson, J. Appl. Phys. **74**, 7369 (1993).

[7] P. M. Hui, H. Ehrenreich, and N. F. Johnson, J. Vac. Sci. Technol. **7**, 424 (1989); P. M. Young and H. Ehrenreich, Phys. Rev. B **43**, 12 057 (1991).

[8] P. M. Young, E. Runge, M. Ziegler, and H. Ehrenreich, Phys. Rev. B **49**, 7424 (1994).

[9] N. F. Johnson, J. Phys. Condens. Matter **2**, 2099 (1990).

[10] M. Braun and U. Rössler, J. Phys. C **18**, 3365 (1985); U. Rössler, Solid State Commun. **49**, 943 (1984); M. Mayen and U. Rössler, Phys. Rev. B **44**, 9048 (1991).

[11] B. F. Levine, C. G. Bethea, G. Hasnain, J. Walker, and R. J. Malik, Appl. Phys. Lett. **53**, 196 (1988).

[12] B. F. Levine, J. Appl. Phys. **74**, R1 (1993).

[13] N. F. Johnson, H. Ehrenreich, and R. V. Jones, Appl. Phys. Lett. **53**, 180 (1988).

[14] T. Duffield, R. Bhat, M. Koza, F. De Rose, D. M. Hwang, P. Grabhe, and S. J. Allen, Phys. Rev. Lett. **56**, 2724 (1986).

[15] H. S. Li, R. P. G. Karunasiri, Y. W. Chen, and K. L. Wang, J. Vac. Sci. Technol. B **11**, 922 (1993).

[16] Y. Hirayama, J. H. Smet, L.-H. Peng, C. G. Fonstad, and E. P. Ippen, Appl. Phys. Lett. **63**, 1663 (1993).

[17] L.-H. Peng, Ph.D. thesis, Harvard University, 1994; L.-H. Peng and C. G. Fonstad, J. Appl. Phys. **77**, 747 (1995).

[18] L. C. Lew Yan Voon, M. Willatzen, M. Cardona, and L. R. Ram-Mohan (unpublished).

[19] P.-O. Löwdin, J. Math. Phys. **3**, 969 (1962).

[20] Another parameter neglected in our treatment is the so-called off-diagonal spin-orbit coupling $\Delta^- = 3\langle 7,0|H|13,0\rangle$. For GaAs, $\Delta^- = -0.085$ eV (see Ref. 22).

[21] M. L. Cohen and V. Heine, in *Solid State Physics*, edited by H. Ehrenreich, F. Seitz, and D. Turnbull (Academic, New York, 1969), Vol. 24, p. 37.

[22] M. Cardona, N. E. Christensen, and G. Fasol, Phys. Rev. B **38**, 1806 (1988).

[23] *Semiconductors: Group IV Elements and III-V Compounds*, edited by O. Madelung (Springer, New York, 1991).

[24] N. F. Johnson, Ph.D. thesis, Harvard University, 1989.

[25] E. R. Youngdale, J. R. Meyer, C. A. Hoffman, F. J. Bartoli, C. H. Grein, P. M. Young, H. Ehrenreich, R. H. Miles, and D. H. Chow, Appl. Phys. Lett. **64**, 3160 (1994).

[26] N. F. Johnson and H. Ehrenreich, Surf. Sci. **228**, 197 (1990).

[27] A. Shik, in *Intersubband Transitions in Quantum Wells*, edited by E. Rosenchen, B. Vintner, and B. Levine (Plenum, New York, 1992).

[28] H. Ehrenreich and H. R. Philipp, Phys. Rev. **128**, 1622 (1962).
[29] B. Vintner and L. Thibaudeau, in *Intersubband Transitions in Quantum Wells* (Ref. 27).
[30] M. Z. Tidrow, K. K. Choi, A. J. De Anni, and W. H. Chang (unpublished); M. Z. Tidrow, K. K. Choi, C. W. Farley, and F. Chang, Appl. Phys. Lett. **65**, 2996 (1994).
[31] E. T. Yu, J. O. McCaldin, and T. C. McGill, in *Solid State Physics*, edited by H. Ehrenreich and D. Turnbull (Academic, Boston, 1992), Vol. 46, p. 1.